# Magnetoconductance, Quantum Hall Effect, and Coulomb Blockade in Topological Insulator Nanocones

Raphael Kozlovsky, Ansgar Graf, Denis Kochan, Klaus Richter, Cosimo Gorini[1]

[1] *Institut für Theoretische Physik, Universität Regensburg, 93053 Regensburg, Germany*

(Dated: October 1, 2019)

Magnetotransport through cylindrical topological insulator (TI) nanowires is governed by the interplay between quantum confinement and geometric (Aharonov-Bohm and Berry) phases. Here, we argue that the much broader class of TI nanowires with varying radius – for which a *homogeneous* coaxial magnetic field induces a *varying* Aharonov-Bohm flux that gives rise to a non-trivial mass-like potential along the wire – is accessible by studying its simplest member, a TI nanocone. Such nanocones allow to observe intriguing mesoscopic transport phenomena: While the conductance in a perpendicular magnetic field is quantized due to higher-order topological hinge states, it shows resonant transmission through Dirac Landau levels in a coaxial magnetic field. Furthermore, it may act as a quantum magnetic bottle, confining surface Dirac electrons and leading to Coulomb blockade. We show numerically that the above-mentioned effects occur for experimentally accessible values of system size and magnetic field, suggesting that TI nanocone junctions may serve as building blocks for Dirac electron optics setups.

Electronic transport across phase-coherent structures has been a central topic of solid state research ever since the birth of mesoscopic physics some 40 years ago. While the complexity of mesoscopic setups has steadily increased, from the simple gate-defined quantum point contacts of the '80s [1] to elaborate present-day electron optics circuits in semiconductors [2] and graphene [3, 4], their structure remains in the vast majority of cases planar – *i.e.* transport takes place in flat two-dimensional (2D) space. Exceptions to the 2D scenario are samples based on carbon nanotubes and 3D topological insulator (3DTI) nanowires [5–8]. 3DTIs are bulk band insulators hosting protected 2D surface metallic states à la Dirac [9]. In mesoscopic nanostructures built out of 3DTIs low-temperature phase-coherent transport takes place on a 2D Dirac metal wrapped around an insulating 3D bulk. As such, it is strongly dependent on a peculiar conjunction of structural (real space) and spectral (reciprocal space) geometrical properties. This has remarkable consequences even for the possibly simplest setup, a topological insulator nanowire (TINW) with constant circular cross section in a coaxial magnetic field, shown in Fig. 2(a). The magnetoconductance of such an object is characterized by a non-trivial interplay between two fundamentals of mesoscopic physics: quantum confinement and geometric [Aharonov-Bohm (AB) and Berry] phases [6–8, 10–12].

An interesting twist offered by 3DTIs, which to the best of our knowledge has not been studied so far, is the possibility of engineering shaped TINWs with a variable cross section, *e.g.* truncated topological insulator nanocones (TINCs) as sketched in Fig. 1(a). When a coaxial magnetic field is switched on, shaped TINWs possess the unique feature that surface charge carriers traversing the wire, experience not only a variation of the centrifugal potential, but also a spatially changing AB flux – a property that cannot easily be realized with bulk conductors. As we will show, this gives rise to a flux-induced effective mass potential along the TINC which, in contrast to cylindrical TINWs, does not possess any magnetic field periodicity. Together with Dirac electron physics this implies a variety of interesting mesoscopic transport phenomena, including resonant transport through Dirac Landau levels and magnetically induced Coulomb blockade physics. Due to the non-trivial real space geometry, all such transport regimes can be accessed simply by applying and tuning a homogeneous magnetic field.

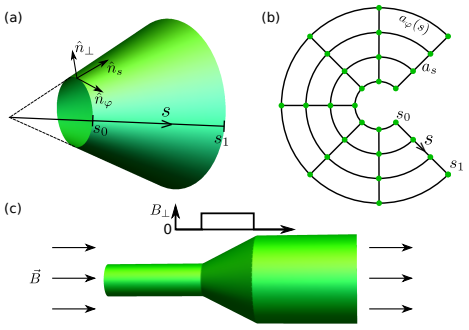


FIG. 1. (a) Sketch of a TINC extended to its conical singularity with local coordinate vectors $\hat{n}_\varphi, \hat{n}_s, \hat{n}_\perp$. (b) Unfolded cone grid used for numerical simulations. (c) TINC in coaxial B-field with cylindrical leads attached, acting as wave guides in magnetotransport simulations.

*Cylindrical TINW in a magnetic field* – For later reference we first consider cylindrical TINWs of radius $R$ in longitudinal [6–8, 10–12] or perpendicular [13–20] magnetic fields. They can be described by the 2D surface Dirac Hamiltonian [21] $H = v_F \left[\frac{1}{2}\left(p_\varphi \sigma_\varphi + \sigma_\varphi p_\varphi\right) + \sigma_z p_z\right]$ with Fermi velocity $v_F$, coordinate along the wire axis $z$, and azimuthal angle $\varphi$. Furthermore, $p_\varphi = \frac{-i\hbar}{R}\partial_\varphi$ and $\sigma_\varphi = \sigma_y \cos\varphi - \sigma_x \sin\varphi$ with $\sigma_x$, $\sigma_y$, $\sigma_z$ the Pauli matrices. With the unitary transformation $U = \exp(i\sigma_z \varphi/2)$,

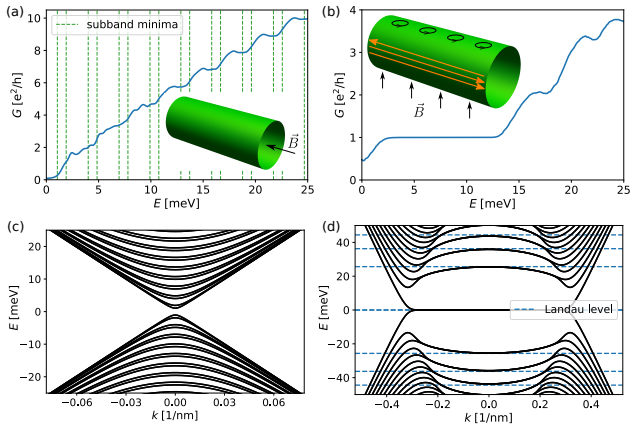


FIG. 2. Disorder averaged conductance (top panels) and band structure (bottom) of a cylindrical TI nanowire in a longitudinal (left panels) and perpendicular (right panels) magnetic field $B = 2\,\mathrm{T}$. See main text for a detailed discussion. Wire size: length $L = 600\,\mathrm{nm}$, circumference $C = 700\,\mathrm{nm}$. Average based on Gaussian disorder is taken over 600 configurations.

the Hamiltonian simplifies to $H = v_F\,(\sigma_z p_z + \sigma_y p_\varphi)$, while the Dirac electron wave functions acquire antiperiodic boundary conditions. The associated Berry phase [22] shifts the angular momentum quantization condition by $\hbar/2$, yielding a gapped subband spectrum $E_l(p_z) = \pm v_F\sqrt{p_z^2 + \hbar^2(l+1/2)^2/R^2}$, with angular momentum quantum number $l \in \mathbb{Z}$. The magnetic field $\mathbf{B}$ is introduced via minimal coupling, $\mathbf{p} \to \mathbf{p} + e\mathbf{A}(z,\varphi)$. For a coaxial $B$-field generating a magnetic flux $\Phi = \pi R^2 B$ (where $B = |\mathbf{B}|$) through the tube the problem remains separable and reduces to that of an electron in an AB ring – the cylinder cross section – times free longitudinal motion. The discrete spectrum of the ring is periodic in $\Phi_0$ [23], and is turned into a series of 1D subbands by the free longitudinal motion. Due to the Berry phase the bands are gapped for $\Phi = n\Phi_0$ and gapless for $\Phi = (n+1/2)\Phi_0, n \in \mathbb{Z}$ [10, 11]. The spectrum is twofold degenerate for integer and half-integer flux, with a non-degenerate gap-crossing mode appearing in the second case. At $\Phi = (n+1/2)\Phi_0$, the gap-crossing "perfectly conducting channel" is predicted to yield an $e^2/h$ conductance plateau. Figure 2(c) shows the generic situation (band gap and non-degenerate levels) with $\Phi \approx 18.86\,\Phi_0$ ($B = 2\,\mathrm{T}$). The corresponding disorder-averaged conductance is depicted in Fig. 2(a), increasing with energy as more channels open for transport [8]. For details of the numerical simulation see below and the Supp. Mat. [24].

If the magnetic field is instead orthogonal to the nanowire axis, the situation changes drastically. The resulting band structure, see Fig. 2(d), can be understood qualitatively in classical terms [25]: The magnetic field component $B_\perp$ perpendicular to the surface varies along the wire circumference, cf. Fig. 2(b). Its magnitude is maximal for $\varphi = 0, \pi$ (cylinder top and bottom) and zero for $\varphi = \pi/4, 3\pi/4$ (sides), where its sign changes. Cyclotron orbits of opposite handedness thus form on the top and bottom surfaces, while "snaking" orbits propagating along the sides appear. Quantum mechanically, the former lead to Landau level (LL) formation, while the latter are chiral 1D hinge states crossing the $B_\perp$-induced gap and signaling a higher-order TI phase [26]. The dashed lines in Fig. 2(d) mark the LL energies for $B_\perp(\varphi = 0)$

$$E_n = \mathrm{sgn}(n)\frac{\hbar v_F}{l_B}\sqrt{2|n|}\;,\; n \in \mathbb{Z}\,, \tag{1}$$

where $l_B = \sqrt{\hbar/[eB_\perp(\varphi=0)]}$ is the magnetic length on the cylinder top and bottom. Around $k = 0$, flat bands represent well-formed LLs, whose dispersion increases with $n$. The upward (downward) bending $n = 0$ subband ensures the existence of a robust conductance plateau $G = e^2/h$ in a large energy window, see Fig. 2(b), where only one chiral hinge state per side is present, and thus no backscattering is possible. The conductance dip close to the Dirac point is treated in Ref. [20].

*TINC in a coaxial magnetic field* – We now generalize our considerations to a TINC as shown in Fig. 1(a), a representative building block of TINWs with varying cross section. We parametrize its surface by the azimuthal angle $\varphi$ and the distance $s$ to the conical singularity. The radius is given by $R(s) = s\,\sin(\beta/2)$, $\beta$ denoting the cone opening angle and $s_0 \le s \le s_1$. After the unitary transformation $U = \exp(i\sigma_z\varphi/2)$, the surface Dirac Hamiltonian reads [27]

$$H = v_F\left[\left(p_s - \frac{i\hbar}{2s}\right)\sigma_z + p_\varphi(s)\sigma_y\right]\,, \tag{2}$$

with $p_\varphi(s) = -\frac{i\hbar}{R(s)}\partial_\varphi$. The spin connection term $-\frac{i\hbar}{2s}$ [28] makes the Hamiltonian (2) Hermitian with respect to the scalar product (with volume form $R(s)\mathrm{d}\varphi\mathrm{d}s$)

$$\langle\Psi_1|\Psi_2\rangle \equiv \int_0^\infty \mathrm{d}s \int_0^{2\pi} \mathrm{d}\varphi\; R(s)\Psi_1^*(s,\varphi)\Psi_2(s,\varphi)\,. \tag{3}$$

We can remove the spin connection term from Eq. (2) via the local transformation $\Psi \to \widetilde{\Psi} = \sqrt{R(s)}\Psi$ and $H \to \tilde{H} = \sqrt{R(s)}H(1/\sqrt{R(s)})$, which also renders the volume form trivial. This yields

$$\tilde{H} = v_F[p_s\sigma_z + p_\varphi(s)\sigma_y]\,, \tag{4}$$

with $\langle\widetilde{\Psi}_1|\widetilde{\Psi}_2\rangle \equiv \int\mathrm{d}s\int\mathrm{d}\varphi\widetilde{\Psi}_1^*(s,\varphi)\widetilde{\Psi}_2(s,\varphi)$, which is not only mathematically convenient, but also necessary for our numerical transport simulations [24].

In presence of a coaxial magnetic field the problem remains rotationally symmetric and thus separable. We proceed via the *exact* separation ansatz $\widetilde{\Psi}_{nl}(s,\varphi) = \mathrm{e}^{i(l+1/2)\varphi}\chi_{nl}(s)$, where $\chi_{nl}(s)$ is a two-component spinor.

Since the azimuthal part of $\Psi_{nl}(s,\varphi)$ is anti-periodic, $l \in \mathbb{Z}$ can still be interpreted as an angular momentum quantum number; the meaning of $n$ will be clarified shortly. Using minimal coupling $p_\varphi(s) \to p_\varphi(s) + eA_\varphi(s)/\hbar$ yields the 1D Dirac equation

$$\left[v_F p_s \sigma_z + V_l(s,B)\sigma_y\right] \chi_{nl}(s) = \epsilon_{nl}\chi_{nl}(s). \tag{5}$$

Here, the angular momentum term

$$V_l(s,B) = \frac{v_F \hbar}{R(s)}\left(l + \frac{1}{2} - \frac{\Phi(s,B)}{\Phi_0}\right), \tag{6}$$

with $\Phi(s,B) = \pi R^2(s) B$, acts as a position-dependent mass potential, and is crucial for predicting the TINC magnetotransport properties – indeed, more generally the properties of arbitrarily shaped, rotationally symmetric TINWs [29]. Its mass-like character becomes evident in Eq. (5), where it couples to $\sigma_y$, while a simple electrostatic potential enters the Dirac equation with the identity matrix. Hence, Eq. (5) describes 1D Dirac electrons feeling the *effective potential* $|V_l(s)|$. While Dirac electrons Klein-tunnel through electrostatic barriers, Klein tunneling through $|V_l(s)|$ is absent. Fig. 3(c) shows $|V_l(s,B)|$ for a given TINC geometry for all $l$-values relevant in the presented energy range (only $l = 15$ and $l = 25$ are colored and labeled, the rest is gray). In transport, an electron injected in mode $l$ "feels" a distinct effective potential $|V_l(s,B)|$. Note that due to the step-like form of $B_\perp(s)$, cf. Fig. 1(c), the situation is similar to single-valley graphene subject to a magnetic step barrier [30, 31].

*Magnetotransport through TINCs* – Our quantum transport simulations including disorder are based on the tight-binding *Python* software package *kwant* [34]. In general, direct discretization of a Hamiltonian with a non-trivial volume form such as Eq. (2) yields a non-Hermitian tight-binding matrix [24]. However, the above transformation $H \to \tilde{H}$ [see Eq. (4)], provides an appropriate basis for the numerical simulations. Conventional discretization of Eq. (4) leads to the effective lattice shown in Fig. 1(b), representing the unfolded cone. The transversal lattice constant $a_\varphi(s)$, which is part of the hopping integral, is adapted such that $N_\varphi a_\varphi(s) = U(s)$, where $N_\varphi$ is the number of lattice points and $U(s)$ the circumference at position $s$, and the ends are "glued" together. Details of the numerical implementation and the Gaussian-correlated disorder model used can be found in [24]. To compute the conductance, highly-doped semi-infinite cylindrical leads with radii $R(s_0)$ and $R(s_1)$ are attached to the conical scattering region, as shown schematically in Fig. 1(c).

Figure 3(a) shows the conductance of a TINC in a coaxial $B$-field with $l_B \ll s_1 - s_0$. Sharp peaks signal resonant transmission through wedge-shaped quasi-bound states of the effective potential: Each wedge (labeled by $l$) hosts a sequence of bound states (labeled by $n$)

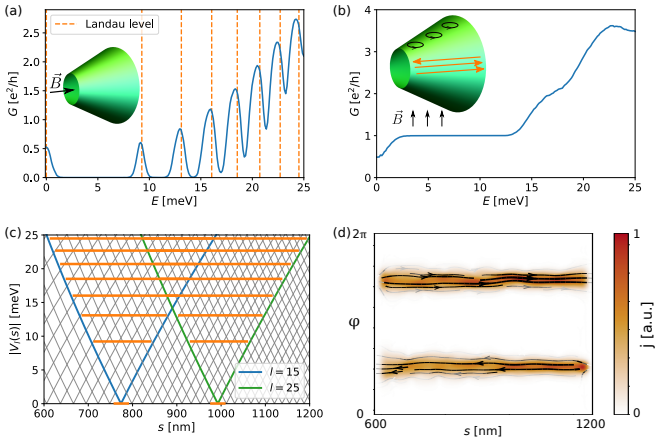


FIG. 3. Disorder averaged TI nanocone conductance for different magnetic field orientations. (a) Coaxial magnetic field: resonant transmission through Landau levels (LLs). Disorder broadens and shifts the LLs from their unperturbed positions, marked by vertical orange dashed lines [32, 33]. The LLs formation (with energies marked as horizontal lines) is depicted in panel (c) and explained in the main text. If energies exceed the effective potentials within the cone, channels fully open for transport and conductance steps of the order of $e^2/h$, slightly deformed by disorder, appear (not shown). (b) Perpendicular magnetic field: the same junction shows a robust conductance plateau due to topologically protected chiral hinge states. The associated current density along the cone is shown in panel (d). Step-like features almost completely smoothed by disorder appear for $E > 13\,\mathrm{meV}$. Parameters: $B = 2\,\mathrm{T}$; cone with (arc) length $s = 600\,\mathrm{nm}$ (see Fig. 1) and opening angle $\theta = 15^\circ$, beginning a distance $s_0 = 600\,\mathrm{nm}$ away from the conical singularity, yielding minimal and maximal circumferences $C_{\min} \approx 492\,\mathrm{nm}$, $C_{\max} \approx 984\,\mathrm{nm}$, respectively. Disorder average is over 600 configurations.

whose energies $\{\epsilon_{nl}\}$, marked by horizontal orange lines in Fig. 3(c), are obtained by solving Eq. (5). The latter are quantum Hall (QH) states, degenerate in $l$ and forming the Dirac LL given in Eq. (1). The degeneracy of a LL can thus be computed by counting the number of wedges within the cone (between $s_0$ and $s_1$). In a perfectly clean TINC degenerate states in adjacent wedges are orthogonal, and hence transport is exponentially suppressed. Finite disorder or surface imperfections, usually present in experimental devices, break rotational symmetry and couple adjacent states leading to broadened resonant tunneling peaks shown in Fig. 3(a). Note the close relation to a QH Corbino geometry [35]: Looking at the TINC from the front, its 2D projection is a ring of finite thickness in a homogeneous perpendicular magnetic field $B_\perp$. In such a Corbino disk geometry we expect transport from the outer to the inner edge to happen via resonant transmission through (Dirac) LLs, provided the field is strong enough for cyclotron orbits to fit within the ring.

For a TINC subject to a $B$-field orthogonal to its symmetry axis, the conductance exhibits completely different

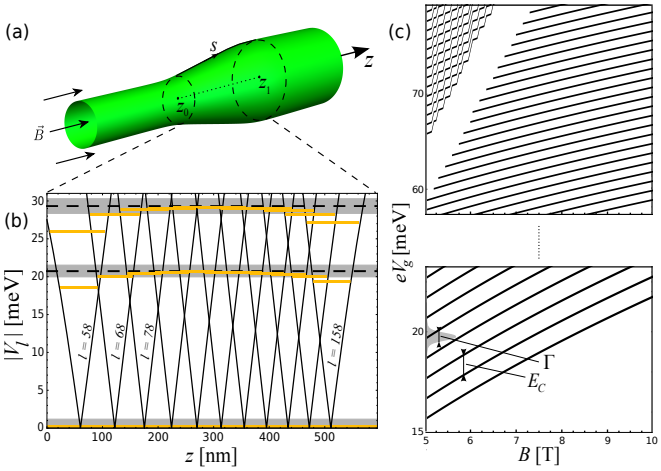


FIG. 4. Coulomb blockade in TI nanocones. (a) Smoothed TINC parametrized by $R_\sigma(z)$ [24], with $\sigma = 0.01$ (small $\sigma$ corresponds to strong smoothing) and $B = 10$ T. (b) $|V_l(z)|$ from $l = 58$ to $l = 158$ (in steps of $\Delta l = 10$) are shown. QH states (marked by orange lines) with $n > 0$ are no longer resonant across the entire junction, leading to tunnel barriers close to $z_0, z_1$. Grey shade depicts the disorder broadening $\Gamma$ from Fig. 3(a). (c) Spectrum (gate voltage $V_g$ dependence) of the Coulomb split LLs (here $n = 1$ and $n = 2$) in the inner part of the smoothed TINC, defined by QH states whose energy lies withing the disorder broadening and are thus resonant in transport.

features, see Fig. 3(b). A dip at zero energy merges into an extended plateau reaching $E \simeq 13$ meV, followed by disorder-smoothed steps at higher energy. As for cylindrical TINW considered before, such features are due to second-order topological hinge states at the sides. If the magnetic length $l_B \ll \pi R(s_0)$, they are indistinguishable from those of a cylindrical TINW, cf. Figs. 2(b) and 3(b). This is actually true in a much more general sense: As long as top and bottom surface provide enough space for LLs to form, the geometry of the TINW in perpendicular B-field is irrelevant for the qualitative conductance features, as opposed to TINWs in coaxial B-field. The current density associated with the lowest-energy hinge state of the TINC, which yields the robust plateau, is plotted in Fig. 3(d) and seen to be chiral – the current on opposite sides ($\varphi = \pi/2, 3\pi/2$) flows in opposite directions.

Notably, the two settings in Fig. 3(a) and (b) correspond to a longitudinal ($\sigma_{xx}$) and transversal ($\sigma_{xy}$) conductivity measurement in a conventional 2D QH setup. In standard QH notation, the longitudinal current density is given by $j_x = \sigma_{xx}E_x + \sigma_{xy}E_y$, $x, y$ denoting the longitudinal and transverse directions. Let us adapt this to the TINC. In a perpendicular magnetic field, $E_x$ vanishes as long as $\epsilon_F$ lies within the plateau due to lack of backscattering. Hence, the conductance is solely determined by $\sigma_{xy}$. On the contrary, in a coaxial magnetic field $E_y$ vanishes since metallic states extend across the circumference, resulting in a conductance determined by $\sigma_{xx}$ only.

*Coulomb blockade in smoothed TINCs* – It can be shown [29] that the form of Eq. (5) and thus the concept of an effective potential along the wire, Eq. (6), is valid more generally for any rotationally symmetric but abritrarily shaped TINWs, the coordinate $s$ simply generalizing to an arc length coordinate. Given the effective potential, one can devise different wire geometries featuring (tunable) magnetic barriers able to confine Dirac electrons [29]. As a simple and paradigmatic example, let us consider a smoother, more realistically shaped TINC, see Fig. 4(a). In the regions of smaller slope (close to the leads) $B_\perp$ rapidly decreases to zero, ergo the QH states are lowered in energy and are no longer resonant with those in the center: a QH island representing a quantum magnetic bottle emerges in the central TINC region between magnetic tunnel barriers close to the leads.

To confirm the above qualitative statements numerically, we consider the setup of Fig. 4(a). For convenience we work with the coaxial coordinate $z$ instead of the arc length $s$. We parametrize the radius $R_\sigma(z)$ such that it reproduces the sharp TINC for $\sigma \to \infty$ [24]. The bound state energies of the individual potential wedges $|V_l(z)|$ obtained by solving the generalized version of Eq. (5) are shown in Fig. 4(b) as orange lines. QH states with $n > 0$ close to the leads are strongly lowered in energy as compared to the central ones, which still form the (disorder-broadened) LLs expected in the limit $\sigma \to \infty$. Only the $n = 0$ LL is unaffected by the smoothing, which is a distinct feature of Dirac electrons. Thus, the conductance through the zeroth LL stays resonant, while potential barriers close to $z_0$, $z_1$ determine transport when the lead Fermi energy aligns with a $n \neq 0$ LL. In the latter case one should be able to observe Coulomb blockade oscillations [36] if the gate voltage $V_g$ of an electrode applied to the central region of the smoothed TINC is varied. The blockade regime requires the smooth TINC border region to be larger than the (local) magnetic length $l_B$, so that off-resonant QH states can form. To fullfill such a requirement we increased the magnetic field to 10 T. Alternatively, a larger TINC or smoother border regions can be used. Finally, a broadening $\Gamma$ smaller than the charging energy $E_c$ is needed to resolve Coulomb-split QH states belonging to a given LL. Figure 4 (c) shows the inner island LL spectrum as function of $B$, black lines representing single QH states, separated by $E_c$ and broadenend by $\Gamma$ (see lower panel). The large gap at $E \approx 60$ meV for $B = 5$ T is the Landau gap between LL $n = 1$ (composed of the lower right set of QH states) and $n = 2$ (upper left set of QH states). For increasing $B$ additional QH states join the $n = 1$ LL, adding to its degeneracy and thus shifting upwards the bottom of the $n = 2$ LL by $E_c$.

*Experimental realization* – The parameters used are within experimental reach: HgTe-based 3DTI tubes [8] or

core-shell nanowires [37] with spatially varying cross sections have already been built for transport experiments. Crucially, our conclusions do not require the TINC to have a truly circular cross section, as is clear from the Corbino disk analogy: Disk deformations lift the degeneracies of the QH states within each LL, but as long as this splitting is smaller then the broadening due to, *e.g.* temperature or disorder, no qualitative conductance change is expected. The charging energy $E_C$ depends on the setup size, geometry and materials, including the dielectrics, and can thus be tuned in a broad range. For example, for a HgTe-based TINC with parameters from Ref. [8] – not optimized for the blockade regime – $E_C$ is already sizeable, of the order of 1 meV.

*Conclusions* – The broad class of shaped TINWs allows for exploring radically different magnetotransport regimes resulting from the interplay between AB and Berry phases, magnetic confinement of Dirac electrons and interactions. The concept of a non-homogeneous effective mass potential arising from a homogeneous applied magnetic field is a central ingredient to understand the shaped TINWs transport properties, irrespective of their specific form. Such properties can be accessed by considering a TINC, for which the simple rotation of the homogeneous magnetic field from coaxial to orthogonal changes its topology both in real and reciprocal space: from a Corbino disk-type geometry with resonant, non-quantized conductance to a QH geometry with second-order topological hinge states, yielding quantized conductance plateaus. Realistically shaped TINCs with smooth connections to the leads further allow to access peculiar Coulomb blockade physics by tuning a coaxial magnetic field. TINCs and junctions thereof could act as building blocks for more complex 3D mesoscopic setups for Dirac electrons – much as quantum point contacts and AB rings are used for planar setups – in particular for hybrid TI-superconducting systems typically used in the search for Majorana fermions [9, 38, 39]. TINCs can also be seen as building units of arbitrarily shaped TINWs [29], where more exotic aspects of QH physics on curved surfaces can be studied [40, 41]. Indeed, in Ref. [41] it was shown for topologically trivial charge carriers that QH states on surfaces with conical singularities are heavily affected by the associated gravitational anomaly. The setting proposed here could be used to experimentally probe such phenomena in transport and for generalization to Dirac-type charge carriers. More generally, the QH physics of fully spin-momentum locked electrons on curved surfaces remains a mostly unexplored field. Shaped TINWs provide an ideal platform to study it, both theoretically and experimentally.

*Acknowledgements* – We thank Dmitry Polyakov and Alex Kamenev for useful discussions. This work was supported by the Deutsche Forschungsgemeinschaft through SFB 1277 (project A07) and within Priority Programme SPP 1666 "Topological Insulators" (project Ri681-12/2). Support by the Elitenetzwerk Bayern Doktorandenkolleg "Topological Insulators" is also acknowledged.

[1] B. J. van Wees, H. van Houten, C. W. J. Beenakker, J. G. Williamson, L. P. Kouwenhoven, D. van der Marel, and C. T. Foxon, "Quantized conductance of point contacts in a two-dimensional electron gas," Phys. Rev. Lett. **60**, 848–850 (1988).

[2] E. Bocquillon, V. Freulon, F. D. Parmentier, J.-M. Berroir, B. Plaçais, C. Wahl, J. Rech, T. Jonckheere, T. Martin, C. Grenier, D. Ferraro, P. Degiovanni, and G. Fève, "Electron quantum optics in ballistic chiral conductors," Ann. Phys. (Berlin) **526**, 1 (2013).

[3] N. Kumada, F. D. Parmentier, H. Hibino, D. C. Glattli, and P. Roulleau, "Shot noise generated by graphene p–n junctions in the quantum Hall effect regime," Nat. Commun. **6**, 8058 (2016).

[4] P. Makk, C. Handschin, E. Tóvári, K. Watanabe, T. Taniguchi, K. Richter, M.-H. Liu, and C. Schönenberger, "Coexistence of classical snake states and Aharonov-Bohm oscillations along graphene $p-n$ junctions," Phys. Rev. B **98**, 035413 (2018).

[5] H. Peng, K. Lai, D. Kong, S. Meister, Y. Chen, X.-L. Qi, S.-C. Zhang, Z.-X. Shen, and Y. Cui, "Aharonov-Bohm interference in topological insulator nanoribbons," Nat. Mater. **9**, 225 (2009).

[6] J. Dufouleur, L. Veyrat, A. Teichgräber, S. Neuhaus, C. Nowka, S. Hampel, J. Cayssol, J. Schumann, B. Eichler, O. G. Schmidt, B. Büchner, and R. Giraud, "Quasiballistic Transport of Dirac Fermions in a $Bi_2Se_3$ Nanowire," Phys. Rev. Lett. **110**, 186806 (2013).

[7] S. Cho, B. Dellabetta, R. Zhong, J. Schneeloch, T. Liu, G. Gu, M. J. Gilbert, and N. Mason, "Aharonov-Bohm oscillations in a quasi-ballistic three-dimensional topological insulator nanowire," Nat. Commun. **6**, 7634 (2015).

[8] J. Ziegler, R. Kozlovsky, C. Gorini, M.-H. Liu, S. Weishäupl, H. Maier, R. Fischer, D. A. Kozlov, Z. D. Kvon, N. Mikhailov, S. A. Dvoretsky, K. Richter, and D. Weiss, "Probing spin helical surface states in topological HgTe nanowires," Phys. Rev. B **97**, 035157 (2018).

[9] N. Z. Hasan and C. K. Kane, "Topological Insulators," Rev. Mod. Phys. **82**, 3045 (2010).

[10] P. M. Ostrovsky, I. V. Gornyi, and A. D. Mirlin, "Interaction-Induced Criticality in $\mathbb{Z}_2$ Topological Insulators," Phys. Rev. Lett. **105**, 036803 (2010).

[11] J. H. Bardarson, P. W. Brouwer, and J. E. Moore, "Aharonov-Bohm Oscillations in Disordered Topological Insulator Nanowires," Phys. Rev. Lett. **105**, 156803 (2010).

[12] J. Dufouleur, E. Xypakis, B. Büchner, R. Giraud, and J. H. Bardarson, "Suppression of scattering in quantum confined 2D helical Dirac systems," Phys. Rev. B **97**, 075401 (2018).

[13] H. Ajiki and T. Ando, "Electronic states of carbon nanotubes," J. Phys. Soc. Jpn. **62**, 1255–1266 (1993).

[14] O. Vafek, "Quantum hall effect in a singly and doubly connected three-dimensional topological insulator," Phys. Rev. B **84**, 245417 (2011).

[15] Y.-Y. Zhang, X.-R. Wang, and X C Xie, "Three-dimensional topological insulator in a magnetic field: chi-

ral side surface states and quantized Hall conductance," J. Phys. Condens. Matter **24**, 015004 (2012), 1103.3761.
[16] M. Sitte, A. Rosch, E. Altman, and L. Fritz, "Topological insulators in magnetic fields: quantum Hall effect and edge channels with a nonquantized $\theta$ term." Phys. Rev. Lett. **108**, 126807 (2012).
[17] L. Brey and H. A. Fertig, "Electronic states of wires and slabs of topological insulators: Quantum hall effects and edge transport," Phys. Rev. B **89**, 085305 (2014).
[18] F. de Juan, R. Ilan, and J. H. Bardarson, "Robust Transport Signatures of Topological Superconductivity in Topological Insulator Nanowires," Phys. Rev. Lett. **113**, 107003 (2014).
[19] E. J. König, P. M. Ostrovsky, I. V. Protopopov, I. V. Gornyi, I. S. Burmistrov, and A. D. Mirlin, "Half-integer quantum Hall effect of disordered Dirac fermions at a topological insulator surface," Phys. Rev. B **90**, 165435 (2014).
[20] E. Xypakis and J. H. Bardarson, "Conductance fluctuations and disorder induced $\nu = 0$ quantum Hall plateau in topological insulator nanowires," Phys. Rev. B **95**, 35415 (2017).
[21] Y. Zhang and A. Vishwanath, "Anomalous Aharonov-Bohm Conductance Oscillations from Topological Insulator Surface States," Phys. Rev. Lett. **105**, 206601 (2010).
[22] G. P. Mikitik and Yu. V. Sharlai, "Manifestation of Berry's Phase in Metal Physics," Phys. Rev. Lett. **82**, 2147 (1999).
[23] U. Eckern and P. Schwab, "Normal persistent currents," Adv. Phys. **44**, 387 (1995).
[24] See Supplemental Material appended at the end.
[25] P. Onorato, "Landau levels and edge states in carbon nanotubes: A semiclassical approach," Phys. Rev. B **84**, 233403 (2011).
[26] See [42]. More precisely, we deal here with a second-order TI phase due to the applied magnetic field, and thus *extrinsic* [16], as opposed to *intrinsic* higher-order phases arising from crystal symmetries [43].
[27] See Ref. [44] for a detailed derivation. The Hamiltonian can most straightforwardly be derived by considering the Dirac operator for spin-1/2 particles on a conical surface, and computing the appropriate spin connection entering the covariant derivative. Details of this procedure can be found in Ref. [28].
[28] M. Fecko, "Differential geometry and lie groups for physicists," (Cambridge university press) (2006).
[29] R. Kozlovsky et al., to be published.
[30] A. De Martino, L. Dell'Anna, and R. Egger, "Magnetic Confinement of Massless Dirac Fermions in Graphene," Phys. Rev. Lett. **98**, 066802 (2007).
[31] M. Ramezani Masir, P. Vasilopoulos, A. Matulis, and F. M. Peeters, "Direction-dependent tunneling through nanostructured magnetic barriers in graphene," Phys. Rev. B **77**, 235443 (2008).
[32] N. M. R. Peres, F. Guinea, and A. H. Castro Neto, "Electronic properties of disordered two-dimensional carbon," Phys. Rev. B **73**, 125411 (2006).
[33] B. Dóra, "Disorder effect on the density of states in Landau quantized graphene," Low Temp. Phys. **34**, 801–804 (2008).
[34] C. W. Groth, M. Wimmer, A. R. Akhmerov, and X. Waintal, "Kwant: A software package for quantum transport," New J. Phys. **16**, 063065 (2014).
[35] Adam Rycerz, "Magnetoconductance of the Corbino disk in graphene," Phys. Rev. B **81**, 121404 (2010).
[36] C. W. J. Beenakker, "Theory of Coulomb-blockade oscillations in the conductance of a quantum dot," Phys. Rev. B **44**, 1646–1656 (1991).
[37] M. Kessel, J. Hajer, G. Karczewski, C. Schumacher, C. Brüne, H. Buhmann, and L. W. Molenkamp, "Cdtehgte core-shell nanowire growth controlled by rheed," Phys. Rev. Materials **1**, 023401 (2017).
[38] A. Cook and M. Franz, "Majorana fermions in a topological-insulator nanowire proximity-coupled to an *s*-wave superconductor," Phys. Rev. B **84**, 201105 (2011).
[39] J. Manousakis, A. Altland, D. Bagrets, R. Egger, and Yoichi Ando, "Majorana qubits in a topological insulator nanoribbon architecture," Phys. Rev. B **95**, 165424 (2017).
[40] D.-H. Lee, "Surface States of Topological Insulators: The Dirac Fermion in Curved Two-Dimensional Spaces," Phys. Rev. Lett. **103**, 196804 (2009).
[41] T. Can, Y. H. Chiu, M. Laskin, and P. Wiegmann, "Emergent Conformal Symmetry and Geometric Transport Properties of Quantum Hall States on Singular Surfaces," Phys. Rev. Lett. **117**, 266803 (2016).
[42] F. Schindler, A. M. Cook, M. G. Vergniory, Z. Wang, S. S. P. Parkin, B. A. Bernevig, and T. Neupert, "Higher-Order Topological Insulators," Sci. Adv. **4** (2018).
[43] M. Geier, L. Trifunovic, M. Hoskam, and P. W. Brouwer, "Second-order topological insulators and superconductors with an order-two crystalline symmetry," Phys. Rev. B **97**, 205135 (2018).
[44] E. Xypakis, J.-W. Rhim, J. H. Bardarson, and R. Ilan, "Perfect transmission in rippled topological insulator nanowires," (2017), arXiv:1712.06478v1.
[45] L. Susskind, "Lattice fermions," Phys. Rev. D **16**, 3031–3039 (1977).
[46] R. Stacey, "Eliminating lattice fermion doubling," Phys. Rev. D **26**, 468–472 (1982).
[47] K. M. Masum Habib, R. N. Sajjad, and A. W. Ghosh, "Modified dirac hamiltonian for efficient quantum mechanical simulations of micron sized devices," Appl. Phys. Lett. **108**, 113105 (2016).

# Supplemental material to the paper

# "Magnetoconductance, Quantum Hall Effect, and Coulomb Blockade in Topological Insulator Nanocones"

Raphael Kozlovsky, Ansgar Graf, Denis Kochan, Klaus Richter, Cosimo Gorini
Institut für Theoretische Physik, Universität Regensburg, D-93040 Regensburg, Germany

## NUMERICAL IMPLEMENTATION

*Kwant* takes as an input tight-binding Hamiltonians of nanostructures and applies the so-called wave function approach to compute their electronic transport properties using the Landauer-Büttiker formalism [34]. Tight-binding Hamiltonians are passed to kwant as "conventional" Hermitian matrices, i.e. finite dimensional matrices which fulfill $(H^*)^T = H$. However, discretizing the continuum Hamiltonian Eq. (2) leads to a tight-binding representation which does not fulfill this condition. Let us clarify that the reason for this is the non-trivial (non-constant, i.e. coordinate dependent) volume form. Consider, for simplicity, a one-dimensional system with real space coordinate $q$ and volume form $\mathrm{d}V = g(q)dq$. On the lattice, we use the shorthand notation $g_i \equiv g(q_i)$ as well as $\Psi_i \equiv \Psi(q_i)$, where $i$ labels the lattice sites. The condition for the Hermiticity of $H$, $\langle\Phi|H\Psi\rangle = \langle H\Phi|\Psi\rangle$, is then given by

$$\sum_{ij} g_i \Phi_i^* H_{ij} \Psi_j = \sum_{ij} g_j \left(H_{ji}\Phi_i\right)^* \Psi_j \tag{10}$$

on the lattice. From Eq. 10, it is, in general, only possible to deduce that $(H^*)^T = H$ if $g(q) = \text{const}$. Hence, we use the local transformation

$$H \to \tilde{H} = \sqrt{g(q)} H (1/\sqrt{g(q)}), \tag{11}$$

$$\Psi \to \tilde{\Psi} = \sqrt{g(q)}\Psi \tag{12}$$

which makes the volume form trivial. This can be easily seen by considering the scalar product

$$\langle\Phi|H\Psi\rangle = \int_{-\infty}^{\infty} \mathrm{d}q\, g \Phi^* H \Psi \tag{13}$$

$$= \int_{-\infty}^{\infty} \mathrm{d}q\, (\sqrt{g}\Phi^*) \left(\sqrt{g} H \frac{1}{\sqrt{g}}\right) (\sqrt{g}\Psi) \tag{14}$$

$$= \int_{-\infty}^{\infty} \mathrm{d}q\, \tilde{\Phi}^* \tilde{H} \tilde{\Psi}. \tag{15}$$

Note that in Eq. 15, $g$ is fully absorbed in the wave functions and the Hamiltonian, the volume form is trivial. Hence, using the transformation Eq. 11 yields a tight-binding Hamiltonian $\tilde{H}$ which fulfills $(\tilde{H}^*)^T = \tilde{H}$.

We implement the magnetic fields via usual Peierls phases and consider standard Gaussian-correlated disorder,

$$\langle V(\mathbf{r}) V(\mathbf{r}')\rangle = K \frac{\hbar v_F}{2\pi\xi^2} e^{-|\mathbf{r}-\mathbf{r}'|^2/2\xi^2}, \tag{16}$$

with disorder strength $K$ and correlation length $\xi$. For our simulations we use $K = 0.1$ and $\xi = 7$ nm. To avoid the fermion doubling problem [45, 46], we use a conventional Wilson mass term. For a recent discussion see Ref. [47]. Note that a Wilson mass affects the specifics of the spin-momentum texture. Such specifics are, however, irrelevant for our charge transport problem.

## SMOOTHED TINC

For the description of a smoothed TINC we choose to work with the coaxial coordinate $z$. We approximate the Heaviside step function by $\Theta_\sigma(z - z') = \frac{1}{2} + \frac{1}{\pi}\arctan[\sigma(z - z')]$, $\lim_{\sigma\to\infty} \Theta_\sigma(z - z') = \Theta(z - z')$. The radius of a junction that starts with a cylinder of radius $R_0$ at $z = -\infty$ and becomes a cylinder of radius $R_1$ at $z = \infty$ with an intermediate smoothed TINC can then be written as

$$\begin{aligned} R_\sigma(z) =& R_0 + (R_1 - R_0)\Theta_\sigma(z - z_1) \\ &+ \mathcal{S}(z - z_0)[\Theta_\sigma(z - z_0) - \Theta_\sigma(z - z_1)], \end{aligned} \tag{17}$$

where $\mathcal{S} = (R_1 - R_0)/(z_1 - z_0)$ is the slope of a TINC with initial radius $R_0$, final radius $R_1$ and length $z_1 - z_0$. The input parameters chosen for Fig. 4 are such that in the limit $\sigma \mapsto \infty$ the function (17) agrees with the TINC studied in Fig. 3. Thus $R_0 = C_{\min}/(2\pi) = 78.3\,\text{nm}$, $R_1 = 2R_0 = C_{\max}/(2\pi) \approx 156.6\,\text{nm}$, $z_0 = 0$ and $z_1 = 594.7\,\text{nm}$.